materials

MDPI

Article

First–Principles Investigation of the Structural, Elastic, Electronic, and Optical Properties of α– and β–SrZrS$_3$: Implications for Photovoltaic Applications

Henry Igwebuike Eya [1], **Esidor Ntsoenzok** [1,2] and **Nelson Y. Dzade** [1,3,*]

[1] Department of Material Science and Engineering, African University of Science and Technology, Km 10 Airport Road, Galadimawa, Abuja F.C.T. 900107, Nigeria; heya@aust.edu.ng (H.I.E.); esidor.ntsoenzok@cnrs-orleans.fr (E.N.)

[2] CEMHTI–CNRS Site Cyclotron, 3A rue de la Férollerie, 45071 Orléans, France

[3] The School of Chemistry, Cardiff University, Cardiff CF10 3AT, Wales, UK

* Correspondence: DzadeNY@cardiff.ac.uk

Received: 11 January 2020; Accepted: 28 January 2020; Published: 21 February 2020

Abstract: Transition metal perovskite chalcogenides are attractive solar absorber materials for renewable energy applications. Herein, we present the first–principles screened hybrid density functional theory analyses of the structural, elastic, electronic and optical properties of the two structure modifications of strontium zirconium sulfide (needle–like α–SrZrS$_3$ and distorted β–SrZrS$_3$ phases). Through the analysis of the predicted electronic structures, we show that both α– and β–SrZrS$_3$ materials are direct band gaps absorbers, with calculated band gaps of 1.38, and 1.95 eV, respectively, in close agreement with estimates from diffuse–reflectance measurements. A strong light absorption in the visible region is predicted for the α– and β–SrZrS$_3$, as reflected in their high optical absorbance (in the order of 10^5 cm^{-1}), with the β–SrZrS$_3$ phase showing stronger absorption than the α–SrZrS$_3$ phase. We also report the first theoretical prediction of effective masses of photo-generated charge carriers in α– and β–SrZrS$_3$ materials. Predicted small effective masses of holes and electrons at the valence, and conduction bands, respectively, point to high mobility (high conductivity) and low recombination rate of photo-generated charge carriers in α– and β–SrZrS$_3$ materials, which are necessary for efficient photovoltaic conversion.

Keywords: earth–abundant materials; chalcogenide perovskites; Solar cell; Density Functional Theory; Optoelectronic properties

1. Introduction

Perovskite materials have attracted significant attention from researchers due to their potential in various applications. In photovoltaic applications, inorganic–organic halide perovskite materials represent a great breakthrough in the development of solar cell materials with the power conversion efficiency rising from 3.6 to about 24%, since the first application in 2009 by Kojima et al. [1]. The recently reported efficiencies are comparable to the most advanced thin film solar cells, such as CdTe, GaAs, as well as the silicon-based solar cells. In addition to this unprecedented improvement in power conversion efficiency are the ease and low-cost of synthesis of the materials, as well as the fabrication of the solar cell device. Notwithstanding the rapid increase in their efficiencies, the toxicity of the lead content and the intrinsic instability of the bulk lead–halide perovskite materials and their interface heterostructures remain significant drawbacks to their large–scale applications and commercialization [2–5]. These concerns have motivated the search for new absorber materials, that are lead–free but with similar electronic and optical properties as lead–halide perovskite materials. Efforts to replace the Pb in lead halide perovskites with low toxic cations including Sn (II) [6], Ag (I) [7], Bi (III) [8,9], Ti (IV) [10] and Sb (III) [10] have, therefore, received significant attention. These materials yielded non–toxic but low efficiency devices, a maximum of 9% power conversion efficiency (PCE) for the Sn based perovskite. Oxide perovskites on the other hand have proven to have higher stability, due to their resistance to moisture[3], and have been reported to be promising solar absorbers if engineered to have the band gap matched with the solar spectrum [11,12].

Chalcogenide perovskites having the structure ABX_3 (X = S, Se; A, B = metals with combined valence of 6), have recently been proposed for photovoltaic application [13]. Compared to lead halide perovskites, chalcogenide perovskites materials are more environmentally friendly (component elements are earth–abundant and non–toxic) and possess superior electronic and optical properties, suggesting their potential ideal for low–cost tandem solar cell application. So far, a number of transition metal chalcogenide perovskites have been successfully synthesized experimentally and investigated theoretically [3,13–17]. Sun et al. [3] in their theoretical studies, predicted that the band gaps of $CaTiS_3$ (1.0 eV), $BaZrS_3$ (1.75 eV), $CaZrSe_3$ (1.3 eV), and $CaHfSe_3$ (1.2 eV) having the distorted perovskite structure are suitable for making single–junction solar cells. They are generally n–type semiconductors, with thin–films of $BaZrS_3$ recently to have carrier densities in the range of 10^{19}–10^{20} cm^{-3} [18]. Chalcogenide perovskites also display high optical absorption properties, making them promising materials used in addressing the instability and toxicity issues associated with halide perovskites. A number of chalcogenide perovskites including $CaZrS_3$, $SrTiS_3$, $SrZrS_3$ and $BaZrS_3$ have been successfully synthesized by Perera et al. [17] using high temperature sulfurization of their oxide counterparts. A widely tunable bandgap range of 1.73–2.87 eV was reported for these materials. Ju et al. [14] predicted a series of chalcogenide perovskites such as $SrSnSe_3$, $CaSnS_3$ and $SrSnS_3$ with tunable direct bandgaps within the optimal range of 0.9–1.6 eV for single junction solar cell applications. Peng et al. [19] demonstrated, from first–principles density functional theory (DFT) calculations, that the optical transitions near the band edges of chalcogenide perovskites differ from those of their halide counterparts.

Single crystal X–ray diffraction analysis of strontium zirconium sulfide ($SrZrS_3$) samples show two structure modifications (needle–like α–$SrZrS_3$ and distorted β–$SrZrS_3$ phases (Figure 1). The α–and β–$SrZrS_3$ phases both crystallize in the orthorhombic crystal structure with space group *Pnma*. The optical band gaps were estimated to be 1.52 and 2.05 eV for the α–$SrZrS_3$, and β–$SrZrS_3$ phases, respectively, from diffuse–reflectance measurements [16]. Thermal stability investigations by Niu et al. [20] on synthesized α–$SrZrS_3$, β–$SrZrS_3$, $BaZrS_3$, Ba_2ZrS_4 and $Ba_3Zr_2S_7$ show that these chalcogenide perovskites possess excellent thermal stability in air for a temperature range up to 550 °C [16]. The fundamental atomic–level insights into the mechanical and structural characteristics, as well as the electronic and optical features of $SrZrS_3$ materials, albeit, poorly understood and inconclusive. Previous theoretical studies by Oumertem et al. have characterized the electronic and thermodynamic properties of the cubic and orthorhombic $XZrS_3$ (X = Ba, Sr, Ca) compounds, predicting their band gap in the range of 1.151–1.617 eV [15]. There is, however, no systematic theoretical investigation dedicated to elucidating the structural, elastic, and optoelectronic properties of the α–$SrZrS_3$ and β–$SrZrS_3$ chalcogenide perovskites, which makes this investigation timely.

In the present study, we do not only report the structural, mechanical, and electronic properties of α–$SrZrS_3$ and β–$SrZrS_3$ by means of screened hybrid (HSE06) density functional theory methods, but also comprehensively characterized the optical properties and discussed their implications for photovoltaic applications. Based on the calculated optical absorbance, reflectivity, and refractive index, we demonstrate that α– and β–$SrZrS_3$ are suitable solar absorber materials for solar cell and other optoelectronic applications.

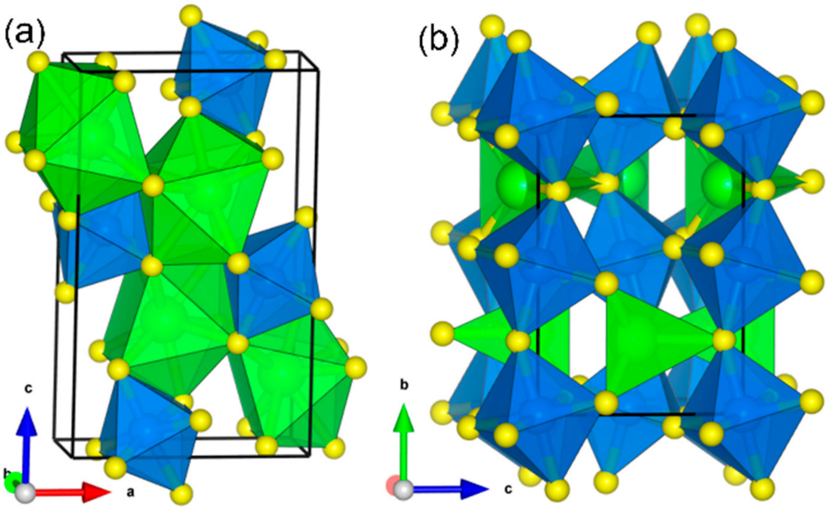

Figure 1. Crystal structure of (**a**) α–$SrZrS_3$ and (**b**) β–$SrZrS_3$. Color code: Sr = Green, Zr = Blue, and S = yellow.

2. Computational Details

The density functional theory (DFT) were performed within periodic boundary conditions as implemented in the Vienna Ab initio Simulation Package (VASP) [21,22]. The Perdew-Burke-Ernzerhof (PBE) generalized gradient approximation (GGA) functional [23] was used for geometry optimizations, while for electronic structures and optical calculations, the screened hybrid functional HSE06 with 25% Hartree−Fock exchange and screening parameter of ω = 0.11 bohr $^{-1}$ was employed [24]. The projected augmented wave (PAW) method was used to describe the interactions between the valence electrons and the cores [25]. Long–range van der Waals (vdW) were accounted for using of the Grimme (DFT–D3) method [26]. A plane–wave basis, set with a kinetic energy cut–off of 600 eV, was tested to be sufficient to converge the total energy of the α–$SrZrS_3$ and β–$SrZrS_3$ phases to within 10^{-6} eV and the residual Hellmann–Feynman forces on all relaxed atoms reached 10^{-3} eV Å^{-1}. The Brillouin zone of the α–$SrZrS_3$ and β–$SrZrS_3$ phases was sampled using 5 × 7 × 3, and 5 × 3 × 5 Monkhorst–Pack [27] K–points mesh, respectively.

The optical properties of α–$SrZrS_3$ and β–$SrZrS_3$ were determined from the complex dielectric function, $\varepsilon(\omega) = \varepsilon_1(\omega) + i\ \varepsilon_2(\omega)$ within the independent–particle formalism [28], where the the imaginary part of the dielectric function is calculated in the long wavelength q→0 limit as,

$$\begin{aligned}\varepsilon_2(\omega) = \varepsilon_{\alpha\beta}^{(2)}(\omega) &= \frac{4\pi^2 e^2}{\Omega}\lim_{q\to 0}\frac{1}{q^2}\sum_{c,v,k} 2w_k\delta(\epsilon_{ck}-\epsilon_{vk}-\omega) \\ &\quad \times\langle u_{ck+e_\alpha q}|u_{vk}\rangle\langle u_{ck+e_\beta q}|u_{vk}\rangle^*\end{aligned} \tag{1}$$

where, Ω and w_k are the volume of the primitive cell and k–point weights, respectively. The $\epsilon_{ck}(\epsilon_{vk})$ are **k**–dependent conduction (valence) band energies, u_{vk}, u_{ck} are the cell periodic part of the pseudo–wave function and $e_{\alpha,\beta}$ are the unit vectors along the Cartesian directions. From Kramers–Kronig transformations, the real part of dielectric function can be determined from the relation,

$$\varepsilon_1(\omega) = \varepsilon_{\alpha\beta}^{(1)}(\omega) = 1 + \frac{2}{\pi}P\int_0^\infty \frac{\varepsilon_{\alpha\beta}^{(2)}(\omega\prime)\omega\prime}{\omega'^2-\omega^2+i\eta}d\omega' \tag{2}$$

where P denotes the principle value. A small value of 0.1, which is acceptable for most calculations was used for the complex shift (η) to smoothen the real part of the dielectric function. The optical parameters, such as absorption coefficient, are based on ε_1 and ε_2. The absorption coefficient (α_{abs}) is calculated using the following relation:

$$\alpha_{abs} = \sqrt{2}\omega\left(\sqrt{\varepsilon_1^2(\omega) + \varepsilon_2^2(\omega)} - \varepsilon_1(\varepsilon)\right)^{1/2}. \tag{3}$$

Local field and excitonic effects have been neglected in the present study as they are not accurately treated in the independent–particle formalism. These effects may be accounted for by using expensive methods, such as Bethe–Salpeter equation (BSE) and time–dependent DFT with proper exchange–correlation kernels [29].

The elastic stiffness constants were calculated using the stress–strain method [30]. The strain (σ) and stress (ε) are related according to Hook's law by $\sigma_i = C_{ij}\varepsilon_j$, where C_{ij} are the elastic stiffness constants. For an orthorhombic system, there are nine independent elastic constants viz; C11, C22, C33, C12, C13, C23, C44, C55 and C66. These elastic constants are used to predict the bulk modulus (B_V) and the shear modulus (G_V). Whereas, Young's modulus (E) and the Poisson's ratio (v) are in turn predicted from the calculated bulk and shear moduli. The bulk and shear moduli measure the material's resistance to uniform compression, and shearing strains, respectively. The bulk and shear moduli were calculated using the Voigt approximation [31] which for orthorhombic structures, can be simplified as follows:

$$B_V = \frac{1}{9}(C_{11} + C_{22} + C_{33}) + \frac{2}{9}(C_{12} + C_{13} + C_{23}) \tag{4}$$

$$G_V = \frac{1}{15}(C_{11} + C_{22} + C_{33} - C_{12} - C_{13} - C_{23}) + \frac{1}{5}(C_{44} + C_{55} + C_{66}) \tag{5}$$

The Young's modulus (E) and Poisson's ratio (v), which are characteristic stiffness properties of a material were obtained using the relations: $E = \frac{9BG}{(3B+G)}$ and $\nu = \frac{(3B-2G)}{2(3B+G)}$.

3. Results and Discussion

3.1. Structural Properties

$SrZrS_3$ crystallizes in two structure modifications; α and β–phases, both in the orthorhombic crystal system with space group *Pnma* (Figure 1). The α–$SrZrS_3$ has five independent lattice sites; one Sr, one Zr, and three S sites, whereas in the β–phase, there exist only four positions (one Sr, one Zr, and two S sites) [32]. The α–$SrZrS_3$ structure consists of one–dimensional double chains of edge–sharing ZrS_6 octahedra along the b axis, with Sr atoms in nine–fold coordination with S atoms, forming tri–capped trigonal prisms (Figure 1a) that are interconnected via common triangular faces [32]. Based on powder neutron diffraction analysis, the β–$SrZrS_3$ is said to have a distorted perovskite structure [33]. Unlike the α–phase, the structure of β–$SrZrS_3$ is constituted by three–dimensionally connected corner–sharing Zr octahedra, and Sr atoms which are eightfold coordinated in a bi-capped trigonal prism (Figure 1b). Summarized in Table 1 are the calculated lattice parameters obtained from a full structure optimization at the using PBE and HSE06 functionals, which show good agreement with known experimental data.[32] In the α–phase, each of the ZrS_6 octahedra shares two opposite edges with one another, forming a linear chain which in turn, interconnect in pairs through additional edge–sharing. The Zr–S bonds form the shortest, having a length of 2.45 Å, whereas the longest bond having a length of 2.65 Å, which involves an S atom bonding to three Zr atoms, occurs opposite to the shortest bond. The Sr–S bonds in the α–$SrZrS_3$ phase ranges from 3.06–3.09 Å. Conversely, the ZrS_6 octahedra of the β–phase have all their corners interconnected forming a three–dimensional network, with Zr–S bonds ranging from 2.54 to 2.57 Å, in close agreement with experimental values (Table 1).

Table 1. Lattice constant (Å) and bond lengths (Å) of for α–$SrZrS_3$ and β–$SrZrS_3$.

	α–$SrZrS_3$			β–$SrZrS_3$		
Parameter	**PBE–D3**	**HSE06+D3**	**Experiment [32]**	**PBE+D3**	**HSE06+D3**	**Experiment [32]**
a (Å)	8.551	8.540	8.525	7.133	7.125	7.109
b (Å)	3.814	3.810	3.826	9.783	9.772	9.766
c (Å)	13.930	13.908	13.925	6.752	6.748	6.735
d(Sr–S)	3.06–3.09	3.05–3.09	3.06–3.08	2.99–3.16	2.98–3.21	2.96–3.37
d(Zr–S)	2.45–2.65	2.44–2.63	2.44–2.64	2.54–2.57	2.54–2.56	2.53–2.56

Based on the optimized structures, we have simulated X–ray diffraction (XRD) spectrum of α–$SrZrS_3$ and β–$SrZrS_3$ using the VESTA Crystallographic Software as shown in Figure 2a. We can see that clear differences between the assigned peaks of α–$SrZrS_3$ and β–$SrZrS_3$, which is consistent with the difference in their lattice parameters. All the peaks in the simulated DFT spectrum match very closely with the experimental XRD measurement from the work of Niu et al. [34], as shown (Figure 2b). We consider that the assigned reflection peaks in the DFT XRD spectrum may become useful in clarifying future experiments, for instance to distinguish between the α–$SrZrS_3$ and β–$SrZrS_3$ phases.

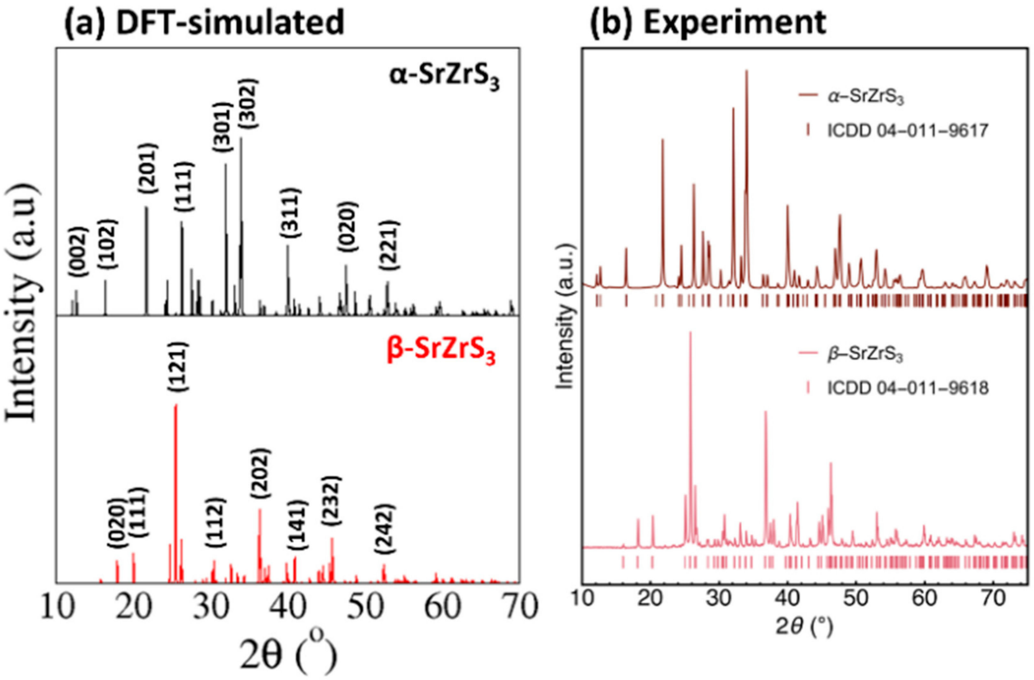

Figure 2. (**a**) DFT–simulated X–ray diffraction pattern of α–$SrZrS_3$ and β–$SrZrS_3$ compared with (**b**) experimental XRD measurement [34].

3.2. Mechanical Properties

The elastic properties of materials give the data necessary in understanding the bonding property between adjacent atomic planes, stiffness, bonding anisotropic and structural stability of the material [35,36]. Shown in Table 2 are the calculated single crystal elastic constants of the α– and β–$SrZrS_3$ materials, all of which satisfy the Born's mechanical stability criteria for orthorhombic structures [37], indicating that both materials are mechanically stable under ambient conditions. The predicted trend of $C_{11} > C_{22} > C_{33}$ for the α–$SrZrS_3$ phase, indicates greater stiffness in the [100] direction than in the [010] and [001] directions. For the β–$SrZrS_3$ phase, $C_{22} > C_{33} > C_{11}$ which implies that β–$SrZrS_3$ is stiffest in the [010] direction and least stiff in the [100] direction. The high elastic stiffness of the α– and β–$SrZrS_3$ could be attributed to strong Sr–S and Zr–S chemical bonding [35]. Summarized in Table 2 are the calculated Bulk (B), shear (G) and Young's (E) moduli. A higher bulk modulus is predicted for the β–SrZrS$_3$ phase (79.9 GPa), similar to the value of 77.35 predicted by Oumertem et al.^{15}, compared to the α–SrZrS$_3$ (61.7 GPa) phase. Similar bulk modulus values were obtained by fitting a third–order Birch–Murnaghan (3rd BM) equation of state (EOS) [38,39] to the DFT–PBE obtained total electronic energy (E) vs unit cell volume (V) data (Figure 3) based on the equation,

$$E(V) = E_0 + \frac{9V_0B_0}{16}\left\{\left[\left(\frac{V_0}{V}\right)^{\frac{2}{3}}-1\right]^3 B_0' + \left[\left(\frac{V_0}{V}\right)^{\frac{2}{3}}-1\right]^2\left[6-4\left(\frac{V_0}{V}\right)^{\frac{2}{3}}\right]\right\} \quad (6)$$

where E_0 and V$_0$ are the equilibrium energy and volume, B_0 is hydrostatic bulk modulus and B′ is the pressure derivative of the bulk modulus at T = 0 K and P = 0 GPa. The bulk modulus and its pressure derivative are calculated at 66.73 GPa and 2.33 for α–SrZrS$_3$ and 83.75 GPa and 2.93 for β–SrZrS$_3$, respectively. This result suggests that the β–SrZrS$_3$ phase is more rigid and less prone to compressive deformation than the α–SrZrS$_3$ phase. Conversely, the α–phase has higher shear and Young's moduli than the β–phase implying more resistance to shear and tensile deformation. The Poisson's ratios (v) are predicted at 0.244 and 0.436 for the α, and β–phases, respectively. The Poisson's ratio allows us to test the ductility/brittleness of material. A material is characterized as ductile if $v < 0.5$, otherwise it is classified as brittle [40]. Based on this criterion, we conclude that both α– and β–SrZrS$_3$ are ductile materials, which implies that any strain-induced defects at the interface, when these materials are deposited on substrates may relax over a relatively short distance.

Table 2. Elastic constants (C$_{ij}$), bulk modulus (B), shear modulus (G), Young's modulus (E), and Poisson's ratio (v) of α–SrZrS$_3$ and β–SrZrS$_3$.

Parameter	**α–SrZrS$_3$**	**β–SrZrS$_3$**
C$_{11}$	137.3	50.3
C$_{22}$	107.4	242.3
C$_{33}$	74.3	118.5
C$_{44}$	32.0	50.9
C$_{55}$	35.4	29.3
C$_{66}$	56.3	8.9
C$_{12}$	44.4	53.1
C$_{13}$	63.6	34.9
C$_{23}$	10.3	66.0
B (GPa)	61.73	79.9
G (GPa)	38.12	34.96
E (GPa)	95.36	91.53
υ	0.244	0.436

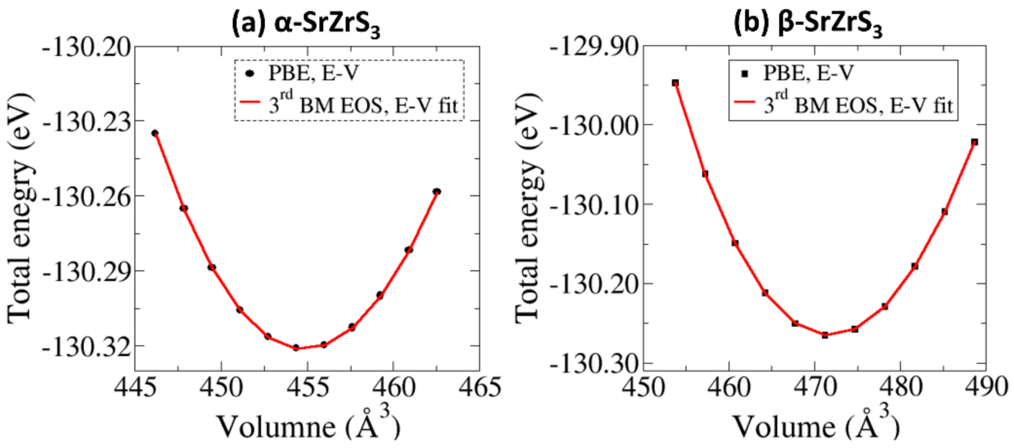

Figure 3. The third–order Birch–Murnaghan equation of state (EOS) fitting to the calculated E−V data of (**a**) α–SrZrS$_3$ and (**b**) β–SrZrS$_3$.

3.3. Electronic Properties

Shown in Figure 4a,b are the electronic band structures of the α–$SrZrS_3$ and β–$SrZrS_3$ phases, respectively, with the corresponding density of states projected on the Sr–*d*, Zr–*d* and S–*p* states in Figure 5a,b. Analysis of the band structures reveal that both α– and β–$SrZrS_3$ are direct band gaps absorbers seeing the bottom of the conduction band and the top of the valence band are located at the same crystal momentum (Γ) points on the Brillouin zone. The band gap energies of α– and β–$SrZrS_3$ are predicted at 1.38, and 1.95 eV, respectively. The predicted values are in close agreement with the estimated optical band gaps from diffuse–reflectance measurements: α–$SrZrS_3$ (1.52 eV) and β–$SrZrS_3$ (2.05 eV) [16]. It is evident from the projected density of states (Figure 5a,b) that the conduction band edge, in both phases, is dominated by Zr–*d* states. Whereas, the contribution from S–*p* orbital dominates the valence band edge.

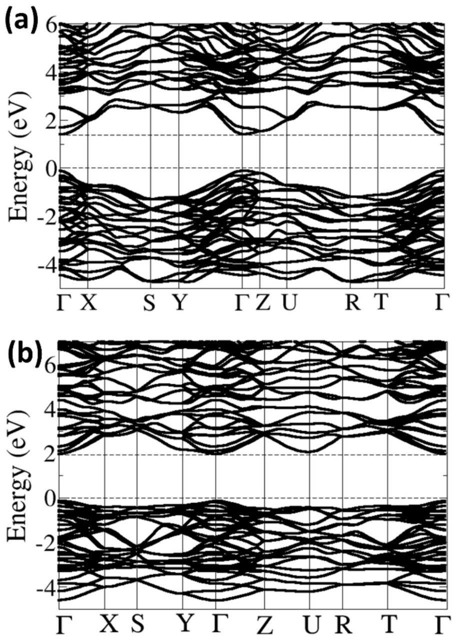

Figure 4. Band structure along the high–symmetry directions of the Brillouin zone of (**a**) α–$SrZrS_3$; and (**b**) β–$SrZrS_3$.

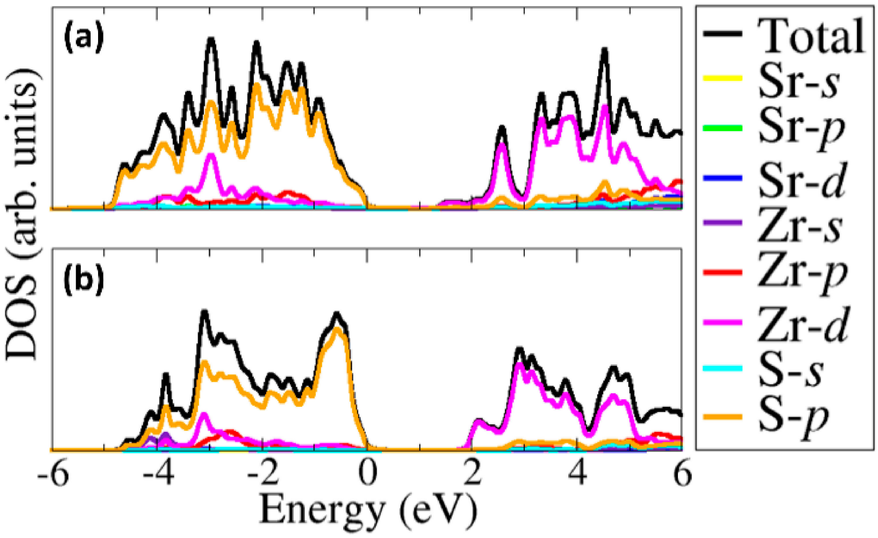

Figure 5. The partial density of states for (**a**) α–$SrZrS_3$; and (**b**) β–$SrZrS_3$.

The charge carrier effective masses (m^*) which is intricately linked to the diffusion coefficient (D) and mobility (μ) of charge carrier in a semiconductor via the relations $D = \frac{k_B T}{e}\mu$ and $\mu = e\frac{\tau}{m^*}$, were also calculated for the α– and β–SrZrS$_3$ materials. Small photo-carrier effective masses result in increased μ and D. The conductivity of charge carrier effective mass dictates the electrical resistivity and optical response of solar devices; hence their calculation is important [41]. Whiles effective masses can be quite difficult to obtain experimentally, accurate DFT calculations [42,43] can complement experiments by computing these properties. The effective masses can be obtained by fitting the energy of the valence band maximum (holes) and conduction band minimum (electrons) to a quadratic polynomial in the reciprocal lattice vector k based on the equation $m^*_{e(h)} = \pm\hbar^2\left(\frac{d^2E_k}{dk^2}\right)^{-1}$. In Table 3 the calculated electron and hole effective masses for the α– and β–SrZrS$_3$ materials are summarized in some selective directions of the Brillouin zone. The predicted smaller, and therefore, the light mass charge carriers correspond to a high mobility of the electrons and holes at the conduction, and valence bands, respectively, and consequently point to high conductivity. The high conductivity also demonstrates the efficient separation of photo-generated charge carriers, which give rise to high-efficiency fabricated solar cell devices. In general, we found that the holes have higher effective masses than electrons in both the α– and β–SrZrS$_3$ materials, suggesting that the electrons do tunnel much readily than the holes. The large effective mass difference between the electrons and holes is an important factor in minimizing their recombination rate [44]. By computing the ratio of the hole to electron effective masses (D = m^*_h/m^*_e), the recombination rate of photo-generated charge carriers can be assessed [45]. Higher D values generally signify higher mobility and a lower recombination rate of the photo-generated charges [46,47]. As shown in Table 3, the highest D values for the α–SrZrS$_3$ phase were calculated along the Y− Γ (26.67), T− Γ (5.25), Z−U (5.00), U−R (3.20), and Γ−X (2.75) directions. For the β–SrZrS$_3$ phase, the highest D values were obtained along the Γ−X (13.50), Z−U (7.40), X−S (4.67), Γ−Z (3.40), Y− Γ (2.36), and U−R (2.33). The higher D values along various directions on the Brillion zone points to efficient separation and low recombination of photo-generated charge carriers in the α– and β–SrZrS$_3$ materials, which is necessary for the fabrication of highly efficient solar device.

Table 3. Calculated hole (m^*_h) and electron (m^*_h) effective masses of α–SrZrS$_3$ and β–SrZrS$_3$ along high symmetry directions.

Material	Direction	m^*_h (m_e)	m^*_e (m_e)	D= m^*_h/m^*_e
α–SrZrS$_3$	Γ−X	0.011	0.004	2.75
	X−S	0.010	0.007	1.43
	S−Y	0.015	0.013	1.15
	Y− Γ	0.080	0.003	26.67
	Γ−Z	0.007	0.005	1.40
	Z−U	0.020	0.004	5.00
	U−R	0.016	0.005	3.20
	R−T	0.023	0.049	0.47
	T− Γ	0.021	0.004	5.25
β–SrZrS$_3$	Γ−X	0.054	0.004	13.50
	X−S	0.014	0.003	4.67
	S−Y	0.017	0.067	0.25
	Y− Γ	0.026	0.011	2.36
	Γ−Z	0.017	0.005	3.40
	Z−U	0.037	0.005	7.40
	U−R	0.007	0.003	2.33
	R−T	0.012	0.015	0.80
	T− Γ	0.009	0.008	1.13

3.4. Optical Properties

The calculated real (dispersive, ε_1) and imaginary (absorptive, ε_2) parts of the dielectric function for α–SrZrS$_3$ and β–SrZrS$_3$ are shown in Figures 6 and 7, respectively. The dielectric constant is predicted at 9.36 for α–$SrZrS_3$ (Figure 6a) and 15.75 β–$SrZrS_3$ (Figure 7a). The predicted high dielectric constants are desired properties for photovoltaics applications as a dielectric constant value of 10 or more is good enough to obtain exciton binding energy (E_b) value lower than 25 meV at room temperature [48]. The absorbance of α–$SrZrS_3$ (Figure 6b) starts at around 1.5 eV, close to its band gap, but with negligible absorption until after 2 eV. The absorption of β–$SrZrS_3$ (Figure 7b) starts at around 2.0 eV, which corresponds to it fundamental band gap. Owing the orthorhombic crystal symmetry of α– and β–$SrZrS_3$, the absorption coefficient, reflectivity and refractive index plotted along the three the crystallographic directions: x, y, and z directions ([100], [010], and [001]) are found to be anisotropic. The absorption coefficient of a material represents its light harvesting ability, which is very necessary as it has great effects on the power conversion efficiency of the resulting solar cells. The high absorption coefficient is desired in solar cell applications. The calculated absorption coefficient, reflectivity and refractive index are shown in Figures 6 and 7. A high absorption coefficient in the order of 10^5 cm^{-1} is predicted for both α– and β–$SrZrS_3$ in the visible light region, which make them suitable for the photovoltaic application. The β–$SrZrS_3$ phase shows stronger absorption around 2 eV than α–$SrZrS_3$ phase.

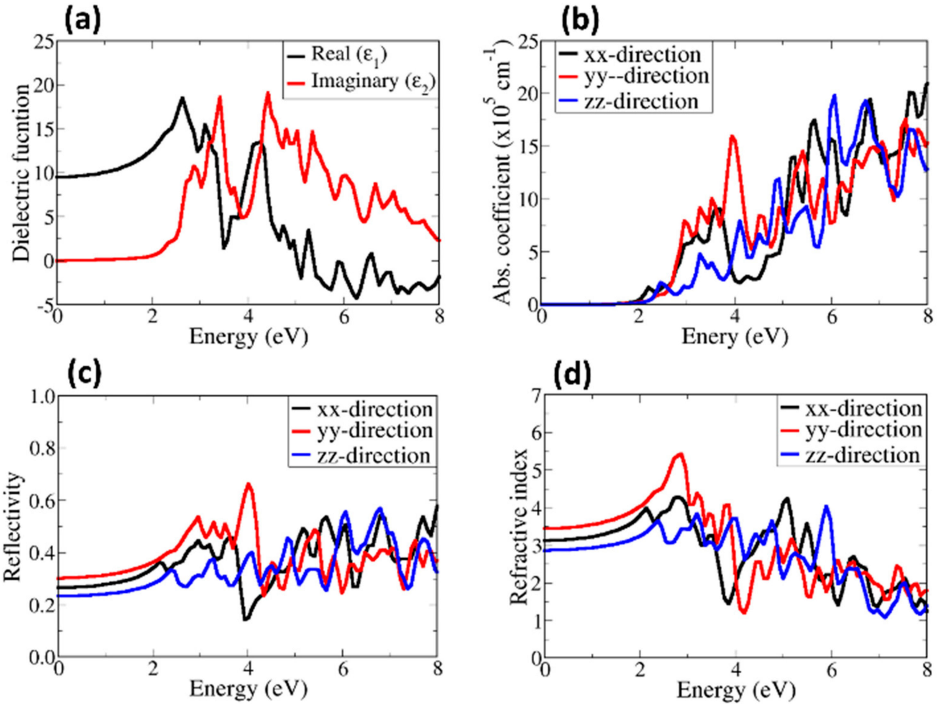

Figure 6. Calculated (**a**) dielectric function, (**b**) absorbance, (**c**) reflectivity and (**d**) refractive index of α–$SrZrS_3$.

The reflectivity and refractive index are two important parameters necessary for solar applications. The reflectivity gives a measure of reflecting light or radiation. When it comes to solar cells, the less the material surfaces reflect a sun's rays, the more energy can be generated. The refractive index of a material, on the other hand, shows its transparency. The optical reflectivity of α–$SrZrS_3$ (Figure 6c) shows a high reflectivity in the y–direction, starts at about 30.2% and reaches a maximum value of about 68.2% at an energy of about 3.8 eV. The static reflectivity in the x, y, and z directions are predicted at about 23%, 30%, and 26%, respectively. This indicate that the least reflection occurs in the z direction. The calculated static reflectivity of β–$SrZrS_3$ (Figure 7c) is predicted to be about 30%, 34% and 38% in the y, z, and x directions, respectively. The reflectivity reaches a maximum (82.2%) at an energy of about 3.5 eV. The high reflectivity in the visible region could cause a significant loss in solar cell efficiency of devices fabricated. Optical losses from reflected light from the front surface can be reduces through surface texturing and anti–reflection coatings. The refractive index is predicted in the range of

2.8–3.5 for α–SrZrS_3 (Figure 6d) and 3.5–4.0 for β–SrZrS_3 (Figure 7d). The calculated refractive indexes for α– and β–SrZrS_3 are similar to the refractive index of Si (η = 3.4 at 550 nm) [49].

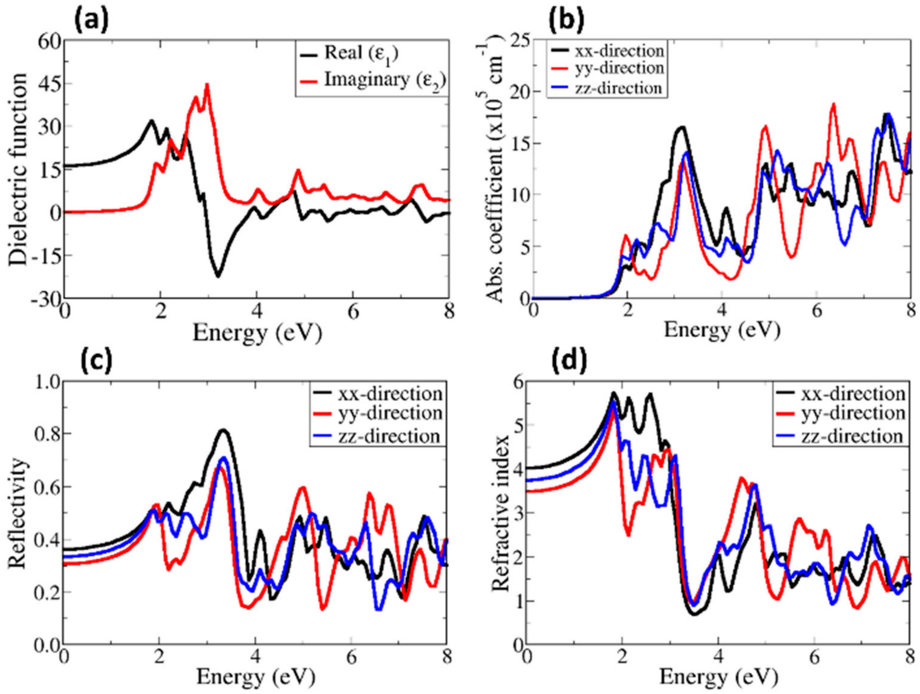

Figure 7. Calculated (**a**) dielectric function, (**b**) absorbance, (**c**) reflectivity and (**d**) refractive index of β–SrZrS_3.

4. Summary and Conclusions

We performed comprehensive first–principles GGA and hybrid DFT investigations the structures and properties α–SrZrS_3 and β–SrZrS_3 transition metal chalcogenide perovskites. Both α– and β–SrZrS_3 materials were demonstrated to be mechanically stable at ambient conditions, based on their calculated single–crystal elastic constants. The predicted electronic structures show that both α– and β–SrZrS_3 are direct band gaps absorbers with band gap of calculated at 1.38, and 1.95 eV, respectively, in close agreement with estimates from diffuse–reflectance measurements. Based on the dielectric functions obtained, we show that α– and β–SrZrS_3 have strong light absorption in the visible region, as reflected in their high optical absorbance (in the order 10^5 cm^{-1}). The β–SrZrS_3 shows a stronger absorption around 2 eV than α–SrZrS_3. The first theoretical prediction of effective masses of photo-generated charge carriers, in α– and β–SrZrS_3 materials, suggest s high-mobility (high-conductivity) and low recombination rate of photo-carriers in these materials, making them attractive for solar cell and other optoelectronic applications.

Author Contributions: H.I.E. performed the DFT simulations and data analysis, and wrote the paper. E.N. and N.Y.D. contributed to the study design and scientific discussion of the results. All co–authors contributed to the manuscript. All authors have read and agreed to the published version of the manuscript.

Funding: This research was funded by the UK's Engineering and Physical Sciences Research Council (EPSRC), grant number EP/S001395/1.

Acknowledgments: H.I.E. acknowledges African University of Science and Technology (AUST) for studentship. This work also made use of the facilities of ARCHER (http://www.archer.ac.uk), the UK's national supercomputing service via our membership of the UK's HEC Materials Chemistry Consortium, which is funded by EPSRC (EP/L000202). We also acknowledge the used of computational facilities of the Advanced Research Computing at Cardiff (ARCCA) Division, Cardiff University, and HPC Wales. Information on the data that underpins the results presented here, including how to access them, can be found in the Cardiff University data catalogue at http://doi.org/10.17035/d.2020.0099250231.

Conflicts of Interest: The authors declare no conflict of interest.

References

1. Kojima, A.; Teshima, K.; Shirai, Y.; Miyasaka, T. Organometal Halide Perovskites as Visible–Light Sensitizers for Photovoltaic Cells. *J. Am. Chem. Soc.* **2009**, *131*, 6050–6051. [CrossRef] [PubMed]
2. Wang, A.J.; Shang, S.L.; Du, Y.; Kong, Y.; Zhang, L.J.; Chen, L.; Zhao, D.D.; Liu, Z.K. Planar Heterojunction Perovskite Solar Cells via Vapor–Assisted Solution Process. *J. Am. Chem. Soc.* **2014**, *136*, 622–625.
3. Sun, Y.; Agiorgousis, M.L.; Zhang, P.; Zhang, S. Chalcogenide Perovskites for Photovoltaics. *Nano Lett.* **2015**, *15*, 581–585. [CrossRef] [PubMed]
4. Noel, N.K.; Stranks, S.D.; Abate, A.; Wehrenfennig, C.; Guarnera, S.; Haghighirad, A.; Sadhanala, A.; Eperon, G.E.; Pathak, S.K.; Johnston, M.B.; et al. Lead–free organic–inorganic tin halide perovskites for photovoltaic applications. *Energy Environ. Sci.* **2014**, *7*, 3061–3068. [CrossRef]
5. Shuyan, S.; Liu, J.; Portale, G.; Fang, H.; Blake, G.R.; Brink, G.H.; Koster, L.A.; Loi, M.A. Highly Reproducible Sn-Based Hybrid Perovskite Solar Cells with 9% Efficiency. *Adv. Energy Mater.* **2018**, *8*, 1702019.
6. Song, T.; Yokoyama, T.; Aramaki, S.; Kanatzidis, M.G. Performance Enhancement of Lead–Free Tin–based Perovskite Solar Cells with Reducing Atmosphere– Assisted Dispersible Additive. *ACS Energy Lett.* **2017**, *24*, 897–903. [CrossRef]
7. Yang, B.; Chen, J.; Yang, S.; Hong, F.; Sun, L.; Han, P.; Pullerits, T.; Deng, W.; Han, K. Lead–Free Silver–Bismuth Halide Double Perovskite Nanocrystals. *Angew. Chem. Int. Ed. Engl.* **2018**, *4*, 5359–5363. [CrossRef]
8. Sanders, S.; Stümmler, D.; Pfeiffer, P.; Ackermann, N.; Simkus, G.; Heuken, M.; Baumann, P.K.; Vescan, A.; Kalisch, H. Chemical Vapor Deposition of Perovskite Films for Solar Cell Application. *Sci. Rep.* **2019**, *9*, 9774. [CrossRef]
9. Durrant, J.R. Green fabrication of stable lead–free bismuth based perovskite solar cells using a non–toxic solvent. *Commun. Chem.* **2019**, *2*, 1–7.
10. Chen, M.; Ju, M.; Carl, A.D.; Zong, Y.; Grimm, R.L.; Gu, J.; Zeng, X.C.; Zhou, Y.; Padture, N. Cesium Titanium (IV) Bromide Thin Films Based Stable Lead–free Perovskite Solar Cells. *Joule* **2018**, *2*, 558–570. [CrossRef]
11. Nechache, R.; Harnagea, C.; Li, S.; Cardenas, L.; Huang, W.; Chakrabartty, J.; Rosei, F. Bandgap tuning of multiferroic oxide solar cells. *Nat. Photon.* **2015**, *9*, 61–67. [CrossRef]
12. Grinberg, I.; West, D.V.; Torres, M.; Gou, G.; Stein, D.M.; Wu, L.; Chen, G.; Gallo, E.M.; Akbashev, A.R.; Davies, P.K.; et al. Perovskite oxides for visible–light–absorbing ferroelectric and photovoltaic materials. *Nature* **2013**, *503*, 509–512. [CrossRef] [PubMed]
13. Meng, W.; Saparov, B.; Hong, F.; Wang, J.; Mitzi, D.B.; Yan, Y. Alloying and Defect Control within Chalcogenide Perovskites for Optimized Photovoltaic Application Alloying and Defect Control within Chalcogenide Perovskites for Optimized Photovoltaic Application. *Chem. Mater.* **2016**, *283*, 821–829. [CrossRef]
14. Ju, M.; Dai, J.; Ma, L.; Zeng, X.C. Perovskite Chalcogenides with Optimal Bandgap and Desired Optical Absorption for Photovoltaic Devices. *Adv. Energy Mater.* **2017**, *8*, 2–8. [CrossRef]
15. Oumertem, M.; Saadi, D.M.; Rai, N.B.D.P.; Ibrir, R.K.M. Theoretical investigation of the structural, electronic and thermodynamic properties of cubic and orthorhombic $XZrS_3$ (X = Ba, Sr, Ca) compounds. *J. Comput. Electron.* **2019**, *2*, 415–427. [CrossRef]
16. Niu, S.; Milam-Guerrero, J.; Melot, B.C. Thermal stability study of transition metal perovskite sulfides. *J. Mater. Res.* **2018**, *24*, 4135–4143. [CrossRef]
17. Perera, S.; Hui, H.; Zhao, C.; Xue, H.; Sun, F.; Deng, C.; Gross, N.; Milleville, C.; Xu, X.; Watson, D.F.; et al. Chalcogenide perovskites – an emerging class of ionic semiconductors. *Nano Energy* **2016**, *22*, 129–135. [CrossRef]
18. Wei, X.; Hui, H.; Zhao, C.; Deng, C.; Han, M.; Yu, Z.; Sheng, A.; Roy, P.; Chen, A.; Lin, J.; et al. Realization of $BaZrS_3$ chalcogenide perovskite thin films for optoelectronics. *Nano Energy* **2020**, *68*, 104317. [CrossRef]
19. Peng, Y.; Sun, Q.; Chen, H.; Yin, W.-J. Disparity of the Nature of the Band Gap between Halide and Chalcogenide Single Perovskites for Solar Cell Absorbers. *J. Phys. Chem. Lett.* **2019**, *10*, 4566–4570. [CrossRef]
20. Niu, S.; Huyan, H.; Liu, Y.; Yeung, M.; Ye, K.; Blankemeier, L.; Orvis, T.; Sarkar, D.; Singh, D.J.; Kapadia, R.; et al. Bandgap Control via Structural and Chemical Tuning of Transition Metal Perovskite Chalcogenides. *Adv. Matter.* **2017**, *29*, 16–21. [CrossRef]
21. Kresse, G.; Hafner, J. Ab initio molecular dynamics for liquid metals. *J. Non. Cryst. Solids* **1995**, *1*, 558–561. [CrossRef]

22. Kresse, G.; Furthmüller, J. Efficient iterative schemes for ab initio total–energy calculations using a plane–wave basis set. *Phys. Rev. B Condens. Matter Mater. Phys.* **1996**, *54*, 11169–11186. [CrossRef] [PubMed]
23. Perdew, J.P.; Ernzerhof, M.; Burke, K. Generalized Gradient Approximation Made Simple. *Phys. Rev. Lett.* **1996**, *18*, 3865–3868. [CrossRef] [PubMed]
24. Krukau, A.V.; Vydrov, O.A.; Izmaylov, A.F.; Scuseria, G.E. Influence of the exchange screening parameter on the performance of screened hybrid functionals. *J. Chem. Phys.* **2006**, *22*, 224106. [CrossRef] [PubMed]
25. Blöchl, P.E. Projector augmented–wave method. *Phys. Rev. B* **1994**, *50*, 17953–17979.
26. Grimme, S.; Antony, J.; Ehrlich, S.; Krieg, H. A consistent and accurate ab initio parametrization of density functional dispersion correction (DFT–D) for the 94 elements H–Pu. *J. Chem. Phys.* **2010**, *132*, 154104. [CrossRef] [PubMed]
27. Pack, J.D.; Monkhorst, H.J. Special points for Brillouin–zone integrations. *Phys. Rev. B* **1977**, *16*, 1748–1749. [CrossRef]
28. Sipe, J.E.; Ghahramani, E. Nonlinear optical response of semiconductors in the independent–particle approximation. *Phys. Rev. B* **1993**, *48*, 11705. [CrossRef]
29. Terentjev, A.V.; Constantin, L.A.; Pitarke, J.M. Gradient–dependent exchange–correlation kernel for materials optical properties. *Phys. Rev. B* **2018**, *98*, 085123. [CrossRef]
30. Zhou, L.; Holec, D.; Mayrhofer, P.H. First–principles study of elastic properties of cubic $Cr_{1-x}Al_xN$ alloys. *J. Appl. Phys.* **2013**, *113*, 043511. [CrossRef]
31. Wu, Z.; Zhao, E.; Xiang, H.; Hao, X.; Liu, X.; Meng, J. Crystal structures and elastic properties of superhard IrN_2 and IrN_3 from first principles. *Phys. Rev. B Condens. Matter Mater. Phys.* **2007**, *76*, 1–15.
32. Lee, C.S.; Kleinke, K.M.; Kleinke, H. Synthesis, structure, and electronic and physical properties of the two $SrZrS_3$ modifications. *Solid State Sci.* **2005**, *7*, 1049–1054. [CrossRef]
33. Lelieveld, R.; IJdo, D.J.W. Sulphides with the $GdFeO_3$ structure. *Acta Crystallogr. Sect. B Struct. Crystallogr. Cryst. Chem.* **1980**, *36*, 2223–2226. [CrossRef]
34. Niu, S.; Milam–Guerrero, J.; Zhuo, Y.; Ye, K.; Zhao, B.; Melot, B.C.; Ravichandran, J. Thermal stability study of transition metal perovskite sulfides. *J. Mater. Res.* **2018**, *33*, 4135–4143. [CrossRef]
35. Edrees, S.J.; Shukur, M.M.; Obeid, M.M. Computational Condensed Matter First–principle analysis of the structural, mechanical, optical and electronic properties of wollastonite monoclinic polymorph. *Comput. Condens. Matter.* **2018**, *14*, 20–26. [CrossRef]
36. Dzade, N.Y.; De Leeuw, N.H. Periodic DFT+U investigation of the bulk and surface properties of marcasite (FeS_2). *Phys. Chem. Chem. Phys.* **2017**, *19*, 27478–27488. [CrossRef]
37. Mouhat, F.; Coudert, F.X. Necessary and sufficient elastic stability conditions in various crystal systems. *Phys. Rev. B. Condens. Matter Mater. Phys.* **2014**, *90*, 224104. [CrossRef]
38. Birch, F. Finite Elastic Strain of Cubic Crystals. *Phys. Rev.* **1947**, *71*, 809. [CrossRef]
39. Murnaghan, F.D. The Compressibility of Media under Extreme Pressures. *Proc. Natl. Acad. Sci. USA* **1944**, *30*, 244. [CrossRef]
40. Angelidi, M.; Vassilopoulos, A.P.; Keller, T. Displacement rate and structural effects on Poisson ratio of a ductile structural adhesive in tension and compression. *Int. J. Adhes. Adhes.* **2017**, *78*, 13–22. [CrossRef]
41. Rasukkannu, M.; Velauthapillai, D.; Vajeeston, P. Computational Modeling of Novel Bulk Materials for the Intermediate–Band Solar Cells. *ACS Omega* **2017**, *2*, 1454–1462. [CrossRef] [PubMed]
42. Riffe, D.M. Temperature dependence of silicon carrier effective masses with application to femtosecond reflectivity measurements. *J. Opt. Soc. Am. B* **2002**, *19*, 1092–1100. [CrossRef]
43. Kim, Y.-S.; Hummer, K.; Kresse, G. Accurate Band Structures and Effective Masses for InP, InAs, and InSb Using Hybrid Functionals. *Phys. Rev. B* **2009**, *80*, 035203. [CrossRef]
44. Bahers, T.L.; Rèrat, M.; Sautet, P. Semiconductors Used in Photovoltaic and Photocatalytic Devices: Assessing Fundamental Properties from DFT. *J. Phys. Chem. C* **2014**, *118*, 5997–6008. [CrossRef]
45. Dong, M.; Zhang, J.; Yu, J. Effect of Effective Mass and Spontaneous Polarization on Photocatalytic Activity of Wurtzite and Zinc–Blende ZnS. *APL Mater.* **2015**, *3*, 104404. [CrossRef]
46. Zhang, H.; Liu, L.; Zhou, Z. First–Principles Studies on Facet–Dependent Photocatalytic Properties of Bismuth Oxyhalides (BiOXs). *RSC Adv.* **2012**, *2*, 9224–9229. [CrossRef]

47. Faraji, M.; Sabzali, M.; Yousefzadeh, S.; Sarikhani, N.; Ziashahabi, A.; Zirak, M.; Moshfegh, A. Band Engineering and Charge Separation in the $Mo_{1-x}W_xS_2/TiO_2$ Heterostructure by Alloying: First Principle Prediction. *RSC Adv.* **2015**, *5*, 28460–28466. [CrossRef]
48. Roknuzzaman, M.; Zhang, C.; Ostrikov, K.; Du, A.; Wang, H.; Wang, L.; Tesfamichael, T. Electronic and optical properties of lead–free hybrid double perovskites for photovoltaic and optoelectronic applications. *Sci. Rep.* **2019**, *9*, 718. [CrossRef]
49. Primak, W. Refractive Index of Silicon. *Appl. Opt.* **1971**, *10*, 759–763. [CrossRef]